ACS APPLIED POLYMER MATERIALS

Article

Cite This: ACS Appl. Polym. Mater. 2020, 2, 487−496

pubs.acs.org/acsapm

Nanoscale Mapping of Thermal and Mechanical Properties of Bare and Metal-Covered Self-Assembled Block Copolymer Thin Films

Alexandros El Sachat,*[,†] Jean Spièce,[‡] Charalambos Evangeli,[‡] Alexander James Robson,[‡] Martin Kreuzer,[†] Maria R. Rodríguez-Laguna,[†] Emigdio Chavez,[†] Marianna Sledzinska,[†] Clivia M. Sotomayor Torres,[†,§] Oleg V. Kolosov,[‡] and Francesc Alzina[†]

[†]Catalan Institute of Nanoscience and Nanotechnology (ICN2), CSIC and BIST, Campus UAB, Bellaterra, 08193 Barcelona, Spain

[‡]Physics Department and Materials Science Institute, Lancaster University, Lancaster LA1 4YB, United Kingdom

[§]ICREA, Passeig Lluis Companys 23, 08010 Barcelona, Spain

Supporting Information

ABSTRACT: We report on the structural, mechanical, and thermal analysis of 40 nm thick polystyrene-*block*-poly(ethylene oxide) (PS-*b*-PEO) block copolymer (BCP) films coated with evaporated chromium layers of different thicknesses (1, 2, and 5 nm). Solvent annealing processes allow the structural control of the BCP films morphology by rearranging the position of the PEO cylinders parallel to the substrate plane. High-vacuum scanning thermal microscopy and ultrasonic force microscopy measurements performed in ambient pressure revealed that coated ultrathin metal layers strongly influence the heat dissipation in the BCP films and the local surface stiffness of the individual BCP domains, respectively. The measured tip−sample effective thermal resistance decreases from 6.1×10^7 to 2.5×10^7 K W^{-1} with increasing Cr film thickness. In addition, scanning probe microscopy measurements allow the thermal and mechanical mapping of the two segregated polymer domains (PEO−PS) of sub-50 nm characteristic sizes, with sub-10 nm thermal spatial resolution. The results revealed the effect of the surface morphology of the BCP and the incorporation of the metal film on the nanoscale thermal properties and volume self-assembly on the mechanical properties. The findings from this study provide insight into the formation of high aspect ratio BCP−metal structures with the more established applications in lithography. In addition, knowledge of the thermal and mechanical properties at the nanoscale is required in emergent applications, where BCPs, or polymers in general, are part of the structure or device. The performance of such devices is commonly related to the requirement of increased heat dissipation while maintaining mechanical flexibility.

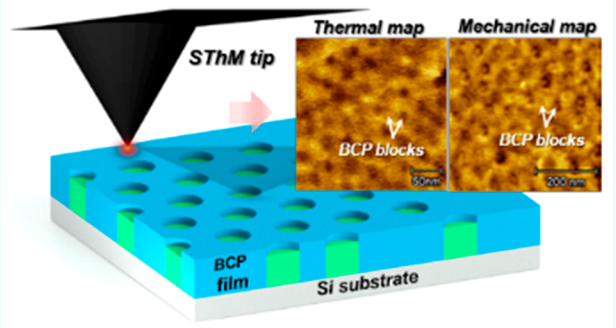

KEYWORDS: *block copolymers, self-assembly, thermal and mechanical mapping, thermal conductivity, scanning probe microscopy*

1. INTRODUCTION

Block copolymers (BCPs) composed of two or more chemically distinct, incompatible blocks are well-known to regularly self-assemble into various ordered nanostructures over macroscopic areas. In thin films, the domain structure is dependent on the interfaces energies (for example, air−BCP and BCP−substrate) and the film thickness, in addition to the other known parameters like composition and molecular weight. The control of the orientation in BCP thin films can be achieved by different approaches including surface modification, solvent annealing, temperature gradient, mechanical and electrical fields, and so on.[1−4]

BCPs are suitable for a number of nanotechnologies on account of the tunability of their size, shape, and composition.[5] Different etch contrast between blocks allows the selective removal of one block and the use of the remaining one as a mask for pattern transfer into a functional material.[6] Hard-mask approaches can be introduced into the nanofabrication process when high-aspect-ratio structures have to be realized,[7−11] such as conductive nanowires and semiconductor nanopillars. Alternatively, the remaining pattern can be employed as a sacrificial soft template structure. Functional materials are then introduced into the pore spaces of sacrificial templates by deposition, followed by removal of the template and generating the desired nanostructure.[12−14] The patterning process can be repeated to produce a stack of 2D patterns, which can be constituted of the same or different materials, morphologies, and orientations.[15] Such block copolymer self-assembly methods have been implemented to pattern microelectronic circuit elements on the nanometer length scale (e.g., high density hard drivers,[16] memory semiconductor capacitors,[17] and magnetic films[18]). Furthermore, BCP (PS-*b*-PEO)

Received: September 30, 2019
Accepted: December 16, 2019
Published: December 16, 2019

DOI: 10.1021/acsapm.9b00924
ACS Appl. Polym. Mater. 2020, 2, 487−496

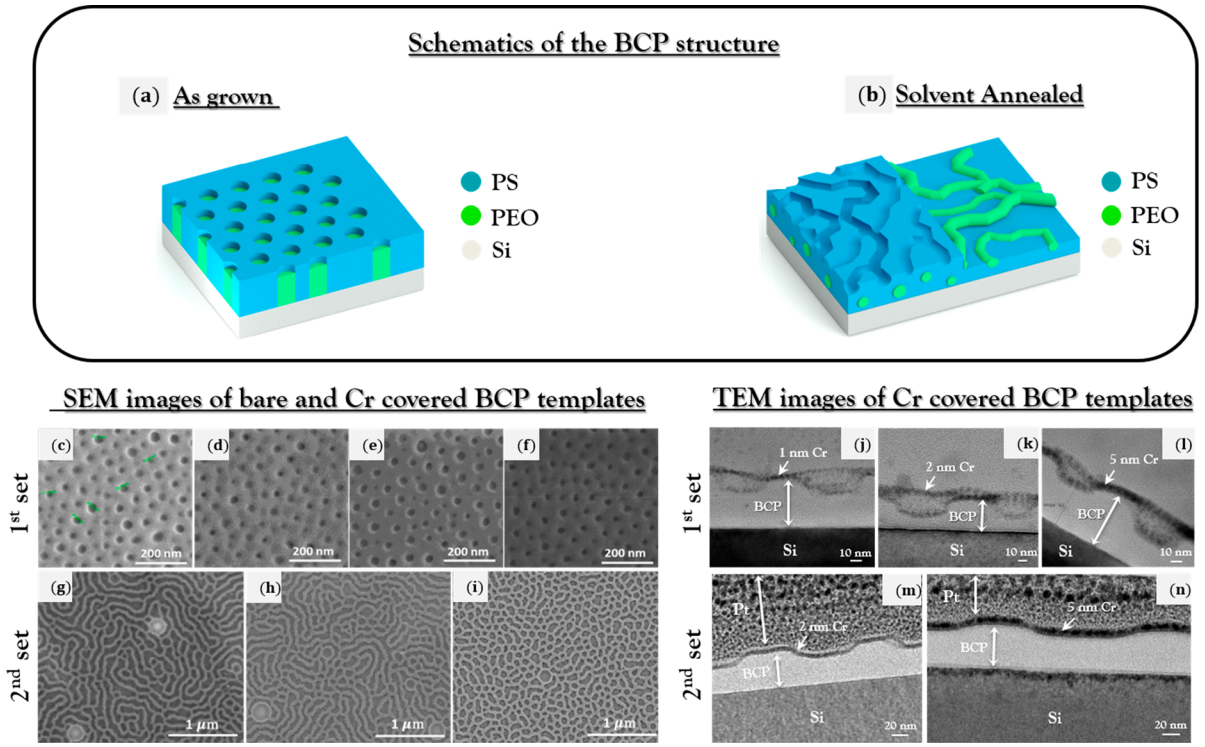

Figure 1. (a, b) Schematics of the BCP films morphology. (c) Top-view SEM image of the fabricated microphase-separated BCP film on Si substrate. (d, e, f) Top-view SEM images of the BCP templates with nominal Cr coatings of 1, 2, and 5 nm (first set of samples), respectively. The darker regions are the PEO domains that were degraded while the lighter regions correspond to the PS matrix. (g) Top-view SEM image of the BCP film after the solvent annealing, showing the modified morphology. (h, i) Solvent-annealed BCP templates with 2 and 5 nm Cr layers, respectively. (j, k, l) Cross-section TEM images of the BCP templates with nominal Cr coatings of 1, 2, and 5 nm, respectively. (m, n) Cross-section TEM images of the solvent-annealed BCP templates with 2 and 5 nm Cr, respectively.

films composed of selectively localized metal nanoparticles recently have been used as transparent patterned electrodes[19] in organic thin film transistors.

Beyond the generation of templates for lithography, the applications of BCPs are expanding to other fields exploiting their functional properties.[20,21] However, there is a need to find complementary properties available from inorganic materials in many cases to enhance existing properties or impart novel functionalities to BCPs.[22,23] Various applications require the deposition of the inorganic materials on the surface of the BCP instead of incorporating the inorganic materials into the phases of the BCP.[24] The selective decoration of evaporated metals has been reported, where nanoparticles and continuous films form by aggregation in the polymer.[10,11,25−31] This provides a route for the metallization of templates; however, it is required to get more insight into the factors and parameters involved in the process.

Metallization in the form of thin films can also be used to improve the heat dissipation in polymer containing active nanoelectronic and optoelectronic devices, where the high thermal resistance of these materials prevents the efficient extraction of heat and may cause the degradation of the organic material.[32] The measurement of the thermal conductance of such polymer-based structures is very important as the polymer layer as well as the polymer−metal or polymer−semiconductor interface can act as a heat barrier in the nanostructure. In addition, the knowledge of heat resistance and thermal stability of self-assembled nanostructures is crucial to define an upper temperature limit for the use of polymers on devices (e.g., to avoid overheating and thermal degradation of the polymer).[33] The possibility given by nanostructuring polymers for further tuning its low thermal conductivity, and combining them with efficient heat conductive materials opens new prospects in the control of heat transport for applications in thermal management.

Contrary to homopolymers, thermal transport in BCP-based systems has been barely explored. George et al.[34] reported thermal transport measurements on BCP films containing PS and poly(methyl methacrylate) (PMMA) polymers (PS-*b*-PMMA). They found that neither the film thickness nor the block's phase separation influenced the effective thermal conductivity of the BCP, obtaining values consistent with the bulk homopolymer values. The authors, however, used an optical diffraction-limited spatial resolution (∼300 nm) technique that is not sufficient to characterize individual BCP blocks only a few nanometers in size. At such highly localized length scales heat transport is affected by interfaces, boundaries, and contacts; thus, the thermal imaging of individual BCP blocks is of high importance.

Furthermore, the mechanical property is arguably the weakest (both figuratively and literally) point of the polymer for applications in nanotechnology, essentially defining the mechanical stability of polymer nanostructure in contact with the nanopatterned metal, especially for polymers structures with high aspect ratios. For instance, in self-assembled structures the presence of a much stiffer block greatly affects microphase separation.[35] In addition, previous works predicted that as the stiffness of one of the blocks is significantly increased, new intermolecular interactions can be introduced,[36,37] influencing the macroscopic structure of the BCP

DOI: 10.1021/acsapm.9b00924
ACS Appl. Polym. Mater. 2020, 2, 487−496

film and thus the nature of thermodynamically stable microphases. In particular, in thin films, these effects can cause significant deviations from the predicted bulk BCP structure and needs to be investigated. Consequently, the nanomechanical mapping of individual phases of the BCP structures is essential to investigate such effects.

The characterization of such complex structures at the nanoscale is crucial for further understanding the morphology−property relationship and the connection between the properties of the constituent components and the structure in the mesoscale. Electron microscopies can simultaneously provide structure characterization and chemical composition. Moreover, atomic force microscopy (AFM)-based techniques, such as ultrasonic force microscopy (UFM) and scanning thermal microscopy (SThM), allow the nanoscale characterization of materials beyond their surface topography and provide surface nanomechanical[38] and thermal[39] properties imaging, respectively.

In this work, we investigated the effect of microphase separation in BCP films on the aggregation of an evaporated metal. Particularly, we studied two different morphologies of these films, which were used as templates for metal coating. The primary BCP morphology consists of vertically oriented PEO cylinders within a PS matrix, which can be transformed in a morphology with in-plane oriented PEO cylindrical domains embedded in a PS matrix by solvent exposure. Structural and chemical characterization was primarily performed to gain insight into the morphology of the heterogeneous structures. Then, we studied the thermal and mechanical properties of the resulting BCP films and the effect of the incorporation of evaporated metal films. The surface imaging and measurements of nanoscale physical properties of these structures, which also revealed subsurface detection and imaging, were performed by SThM and UFM. The complexity and size scale of the samples represent a challenge to the performance of scanning probe microscopy (SPM) for both spatial resolution and probe sensitivity. Moreover, the thermal and mechanical response of the heterogeneous structure reflects the complexity of their morphology, i.e., surfaces, interfaces and film thickness, along with the intrinsic properties of the forming materials.

2. RESULTS AND DISCUSSION

Fabrication and Structural Analysis of BCP Templates. The P-doped Si substrates (Silicon Materials Inc.) were cleaned in an ethanol bath for 1 h and dried under a stream of nitrogen prior to use. Before spin coating the polymer solution, toluene was dispersed three times into the Si substrate and spin-coated at 4000 rpm for 60 s, followed by the same procedure using ethanol. The spin coating (Laurell WS-650-23 comp.) was performed at room temperature (23 °C) and a relative humidity of 40%. A 1% (w/w) solution of PS-*b*-PEO diblock copolymer in toluene with molecular weights of $M_{n,PS}$ = 102 kg mol^{-1} and $M_{n,PEO}$ = 34 kg mol^{-1} was then dispersed into a Si substrate and spin-coated at 4000 rpm for 60 s. The microphase separation of the BCP film by self-assembly resulted in the formation of vertically oriented PEO cylinders showing a hexagonal arrangement embedded in a PS matrix, as seen in previous works using similar methodology.[27,40,41] A schematic of the morphology of the bare BCP film is shown in Figure 1a. Then, we proceeded to deposit Cr on a first set of as prepared BCP templates by using electron beam evaporation (AJA Orion metal evaporator, base pressure ∼2 × 10^{-8} Torr, deposition rate ∼1 A/s, Cr purity ∼99.99%) and targeting Cr layers with different nominal thicknesses (1, 2, and 5 nm).

Figures 1c−f show scanning electron microscopy (SEM) images of the surface of the bare (0 nm Cr) and the three metal decorated BCP samples, respectively (first set of samples). The surface of the bare BCP film shows the presence of cylindrical domains (dark color in SEM) with average radius and average spacing (center-to-center distance) between them of r = 15 ± 2 nm and D = 25 ± 2 nm, respectively. The composition of the cylinders was further verified after performing the thermal and mechanical measurements by selectively etching the PEO block of the bare BCP film with an oxygen plasma.[40,41] (see Figures S2a,b in the Supporting Information). The PS matrix is higher than the PEO cylinders by a difference of 5 ± 1 nm on average. After the evaporation of Cr on the nonetched samples, the oriented polymer template is still distinguishable, which may indicate a preferential metal coverage. This observation will be further confirmed by transmission electron microscopy (TEM) measurements. The rms surface roughness of the BCP films decreases from 3 to 2 nm with increasing Cr layer thickness as estimated from AFM topography images (Figure S3).

A second set of as-prepared BCP templates were processed by solvent annealing in mixed chloroform and toluene atmosphere for 2 h.[42] Here, the samples were enclosed in a sealed chamber with two small vials containing liquid toluene and chloroform, respectively, at room temperature (23 °C) and a relative humidity of 40%. The selective wetting of the minor block of the BCP (hydrophilic PEO) resulted in the alignment of the PEO cylinders parallel to the substrate plane, as has been shown elsewhere.[40] Particularly, the local segregation of the different polymer blocks of PS-*b*-PEO thin films through a solvent annealing process has been studied in previous works.[40,41] A schematic illustration of the morphology of the resulting BCP template is shown in Figure 1b. The rate of the structural conversion is time, temperature, and film thickness dependent, and the microphase separation usually occurs at relatively high solvent concentrations.[27,41,43] Figure 1g shows a SEM image of the solvent annealed BCP film. The brighter color in the SEM images corresponds to the PS matrix while the PEO cylindrical domains are expected to be rearranged horizontally to the film and embedded in the PS matrix.[40,44] Then, similarly to the previous set of samples, Cr layers with nominal thicknesses of 2 and 5 nm were evaporated on the surface of the BCP template by electron beam evaporation (see Figures 1h,i, second set of samples).

To study the morphology and chemical composition of the BCP templates, we performed transmission electron microscopy (TEM), energy dispersive X-ray (EDX), and electron energy-loss spectroscopy (EELS) measurements. Sample cross sections for TEM observation were prepared by conventional grinding and ion milling methodology (first set) or by a focused ion beam on a Zeiss Crossbeam 1540 XB (second set). TEM measurements are shown in Figure 1 while EDX and EELS measurements are presented in Figure S4. In Figures 1j,k,l we show cross-section TEM images of the BCP templates with nominal Cr coatings of 1, 2, and 5 nm, respectively (see first set of samples). The resulting BCP film thickness was measured 39 ± 2 nm. The Cr film is seen to deposit preferentially on the PS matrix, forming islands that grow laterally as the evaporation time increases. The selectivity of Cr is not complete, but a slower kinetics of the growth−coalescence process on PEO cylinders than in the PS matrix

DOI: 10.1021/acsapm.9b00924
ACS Appl. Polym. Mater. 2020, 2, 487−496

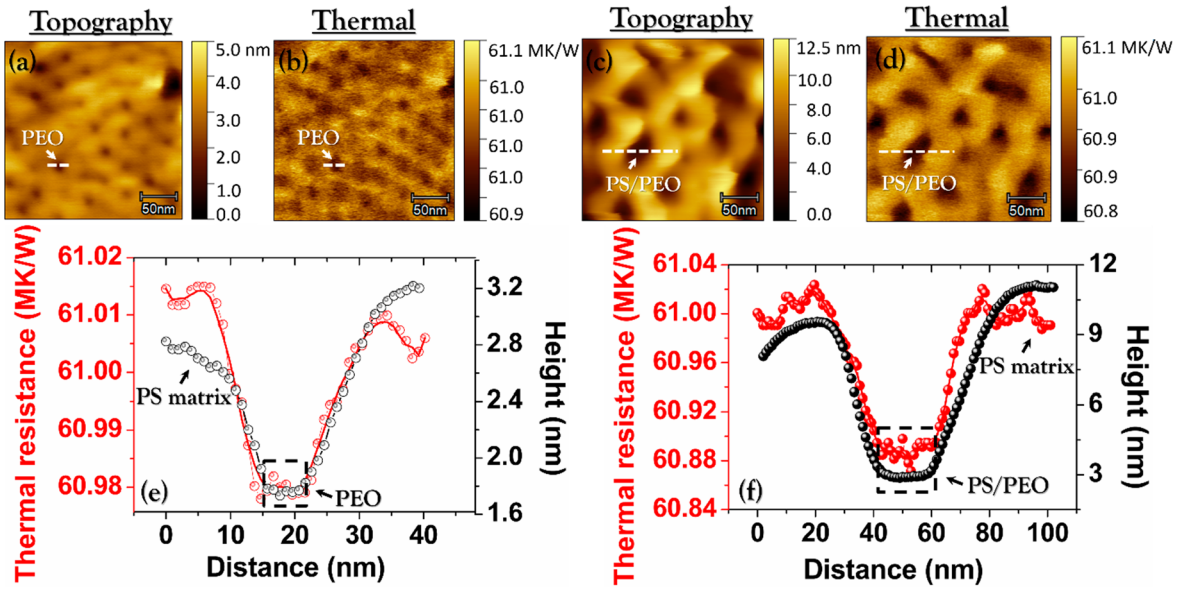

Figure 2. (a, c) Topography and (b, d) thermal resistance maps of the bare BCP films formed by vertical (first set; a, b) and horizontal cylinders (second set; c, d). (e, f) Topography (black data points) and thermal resistance profiles (red data points) along the white dashed lines of (a, c) and (b, d), respectively. Open symbols in (e) correspond to data points from (a, b), and solid symbols in (f) correspond to data points from (c, d).

results in a partial coverage of the PEO cylinders.[45] In addition, the more chemically reactive chains of PEO[31] or PMMA[30] blocks than of the PS matrix hinders metal atom aggregation. The different metal deposition on the two BCP blocks can be seen with higher resolution in STEM mode. In the Supporting Information we show the BCP template with 2 nm thick Cr (first set of samples) in the STEM mode (Figure S5a) and, with higher magnification at the framed area, in Figure S5b. From these images, we observe that the metal layer (see brighter regions in Figure S5b) is preferentially formed on the PS surface. However, the EDX spectrum taken along the line indicated in Figure S5b confirmed the presence of Cr atoms within the PEO domains as well (see Figure S5c).

High-resolution TEM images of the solvent-annealed BCP templates (second set of samples) with nominal 2 and 5 nm thick Cr layers are shown in Figures 1m and 1n, respectively. From the TEM images we observe that there is no selectivity in the deposition of the Cr layer; i.e., a homogeneous Cr layer is evident all along the sample surface. Figure S5d shows the selected area for the composition analysis (orange box) in the BCP template with 2 nm Cr layer. Figures S5e and S5f show the EELS composition maps for chromium and oxygen elements, respectively. As already seen in the TEM images, Figure S5e shows that the Cr layer is homogeneously distributed on top of the BCP surface. The oxygen content (brighter regions in Figure S5f) is clearly detected at the substrate−BCP interface and at the Cr layer. The former is attributed to the native SiO_2 film formed on top of the Si substrate, and the latter reveals the oxidized Cr. EELS composition maps for Cr and O correlate very well, which suggests a full transformed Cr film into oxide. This was corroborated by X-ray induced photoelectron spectroscopy (XPS) (see Figure S6).

From the TEM measurements it is clear that the metal deposition in the two sets of samples has distinctive morphologies. While there is a weak preference of Cr for the matrix surface over cylinders in the first set of samples, in contrast, it fully covers the whole surface of the second set of samples. The uniform metal coverage in the second set of samples suggests surface homogeneity and further supports the description of the parallel oriented cylinders embedded in a PS matrix. A full PS surface is favored as the air−PS interface minimizes the energy of the system.[46] Although the morphology of the metal deposition on the different BCP templates is a necessary information to interpret the thermal and mechanical measurements presented below, further investigation of the basic physical mechanisms of metal film formation on BCP surfaces is beyond the subject of this work. A more detailed discussion regarding the wetting behavior of metal films on solid substrates and their growth kinetics can be found elsewhere.[47,48]

Thermal Analysis of the BCP Templates. Next, we study heat transport between a SThM microscope tip and the fabricated BCP films. Measurements were performed in specialized high vacuum SThM (10^{-7} mbar).[49] Using a doped-Si probe with an integrated resistive heater close to the tip, operating in active mode (described in the Supporting Information), we measured variations of the tip−sample effective thermal resistance in all the BCP samples. More details about the experimental setup and the quantification of the thermal resistance can be found elsewhere.[50] First we study individual regions of the BCP films. In Figure 2, we present topography and thermal images of the bare BCP templates obtained by simultaneous mapping the local variations in height (Figures 2a,c) and tip−sample thermal resistance (Figures 2b,d). The high-resolution thermal image of the BCP template with the vertical cylinder morphology (Figure 2b) shows thermal contrast between the PS matrix and the PEO cylindrical domains, where the hexagonal arrangement of the latter is visible. The PEO cylinders appear darker than the PS matrix in the thermal image, i.e., lower thermal resistance, indicating an increased tip−sample heat transfer when the tip is in contact with the PEO domains.

In particular, from the 40 nm long thermal resistance line profile (white dashed line in Figure 2b), we observe that as the tip is moving from the PS matrix toward the PEO cylinders,

DOI: 10.1021/acsapm.9b00924
ACS Appl. Polym. Mater. 2020, 2, 487−496

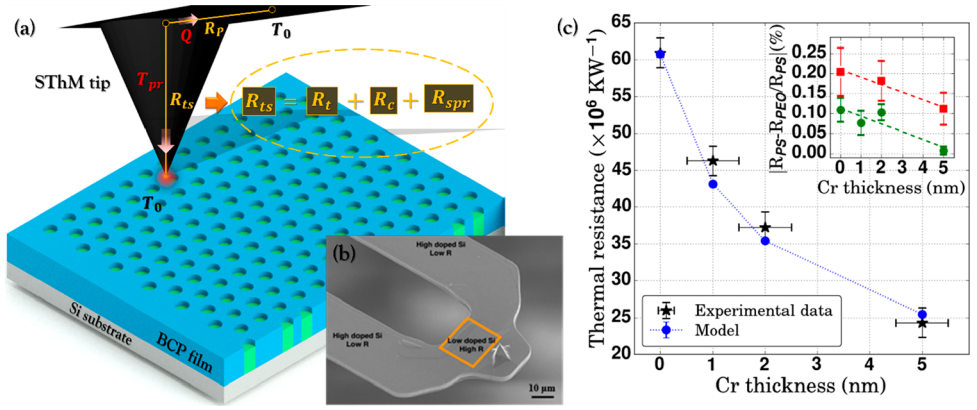

Figure 3. (a) Schematic of the probe−sample thermal resistance model and (b) SEM image of the Si-doped SThM probe. A tip of a nanoscopic radius curvature ((5−10) nm) with a pyramidal shape is mounted on top of the resistive element. (c) The tip−sample thermal resistance variations of the first set of samples as a function of the Cr thickness (black stars) and the two layers on substrate analytical model (blue spheres) with k_1 = 1.7 W m^{-1} K^{-1}, $k_2 = k_{eff}$, $t_2 = t_{eff}$, and $R_t + R_c = 3 \times 10^6$ K W^{-1} (see details in the Supporting Information). The error for the Cr thickness is ±0.5 nm. The inset graph in (c) shows the percentage of the thermal resistance variations between PS and PEO in the BCP films with the vertical (green spheres) and horizontal (red squares) cylinders, respectively.

the thermal resistance decreases ∼0.04 MK/W (see Figure 2e). The same trend has been observed in the full first set of samples, as shown in Figure S7. Similarly, in the BCP film with the embedded horizontal cylinders (Figure 2d), the thermal map shows darker contrast in the depressions than the higher level PS matrix. From the 100 nm long thermal resistance line profile along the white dashed line of Figure 2d, we found that as the tip is moving from the higher level PS matrix toward the depressions, the thermal resistance decreases ∼0.12 MK/W (see Figure 2f). Note that in this case the tip is continuously in contact with the PS matrix while the embedded PEO cylinders cannot be directly probed.

Because the two constituent polymers have similar intrinsic thermal conductivities, the origin of the thermal contrast between the PS matrix and PEO vertical cylinders (see Figure 2b) could be related to a topography artifact. However, by analyzing the topography and thermal resistance profiles of Figures 2e,f, we show that the thermal spatial resolution in our measurements (sub-10 nm range) is sufficient to resolve features with sizes similar to the PEO vertical cylinders. In particular, the thermal lateral resolution is extracted by comparing the slope of the acquired thermal resistance signal, when the tip is moving at the interface between the PS matrix and PEO cylinders, with the corresponding topography, taking the full width at half-maximum as a resolution criterion (see Figure S8), as has been applied in previous AFM-based measurements.[51−53] Therefore, the change of the thermal resistance signal, when the tip is moving from the PS matrix to the PEO cylinders, is not related to the geometrical change of the contact area, mostly ruling out the effect of topography artifacts.

Once topographic artifacts are discarded, a simple explanation of the thermal contrast in the images would be the small difference between the thermal conductivities of the PS and PEO constituent polymers. However, a complete interpretation needs to take into account the heat spreading into the substrate that consequently affects the tip−sample heat transfer. As the BCP film shows a marked surface topography with the vertical PEO cylinders forming surface depressions, it introduces a film thickness modulation, which results, accordingly, in a thermal conductance and thermal contrast change because of different distance between the heater and substrate. The fact that we observe a larger thermal resistance decrease in the depressions in the second set of samples, where larger changes in height are observed (see Figure 2e), further supports the interpretation of a thickness-dependent substrate effect causing the thermal contrast.

We have performed point contact measurements, where the SThM tip is brought in and out of contact with the sample at randomly chosen positions on the BCP samples surfaces to obtain more insightful and quantitative measurements of the effect of deposited Cr on the effective thermal resistance between the tip and the samples. Each point contact measurement gives us the heat flux variation caused by the difference in tip−sample temperature. Then, an averaged effective thermal resistance R_{ts} is obtained for each BCP sample by taking the mean value of the point measurements. In general, for a given sample, R_{ts} can be expressed as a sum of three different thermal resistances:

$$R_{ts} = R_t + R_c + R_{spr} \quad (1)$$

where R_t is the thermal resistance of the SThM conical tip, R_c the thermal interface resistance between tip and the sample in contact (thermal contact resistance), and R_{spr} the thermal spreading resistance within the sample (see schematic in Figure 3a). Particularly, when the probe is in contact with the sample, the heat generated in the SThM heater can only transfer to two heat sinks: the probe cantilever (see Figure 3b) and the sample. By monitoring the change in probe excess temperature ($\Delta T = T_{probe} - T_0$) out ($\Delta T_{nc}$) and in contact ($\Delta T_c$), we measure the effective thermal resistance R_{ts} between the tip and the sample. R_{ts} is given by the following equation:

$$R_{ts} = R_p\left(\frac{\Delta T_{nc}}{\Delta T_{nc} - \Delta T_c} - 1\right) \quad (2)$$

where R_p is the probe thermal resistance, which is measured during the probe calibration procedure (see the Supporting Information) and was found to be $R_p = 8.7 \times 10^4$ K W^{-1}.

In Figure 3c, we show the effective thermal resistance as a function of the Cr thickness in the first set of BCP samples (black stars). It corresponds to the mean value R_{ts} of the measurements taken at each sample and the error bars the dispersion found in the measurements. Note that we measured

DOI: 10.1021/acsapm.9b00924
ACS Appl. Polym. Mater. 2020, 2, 487−496

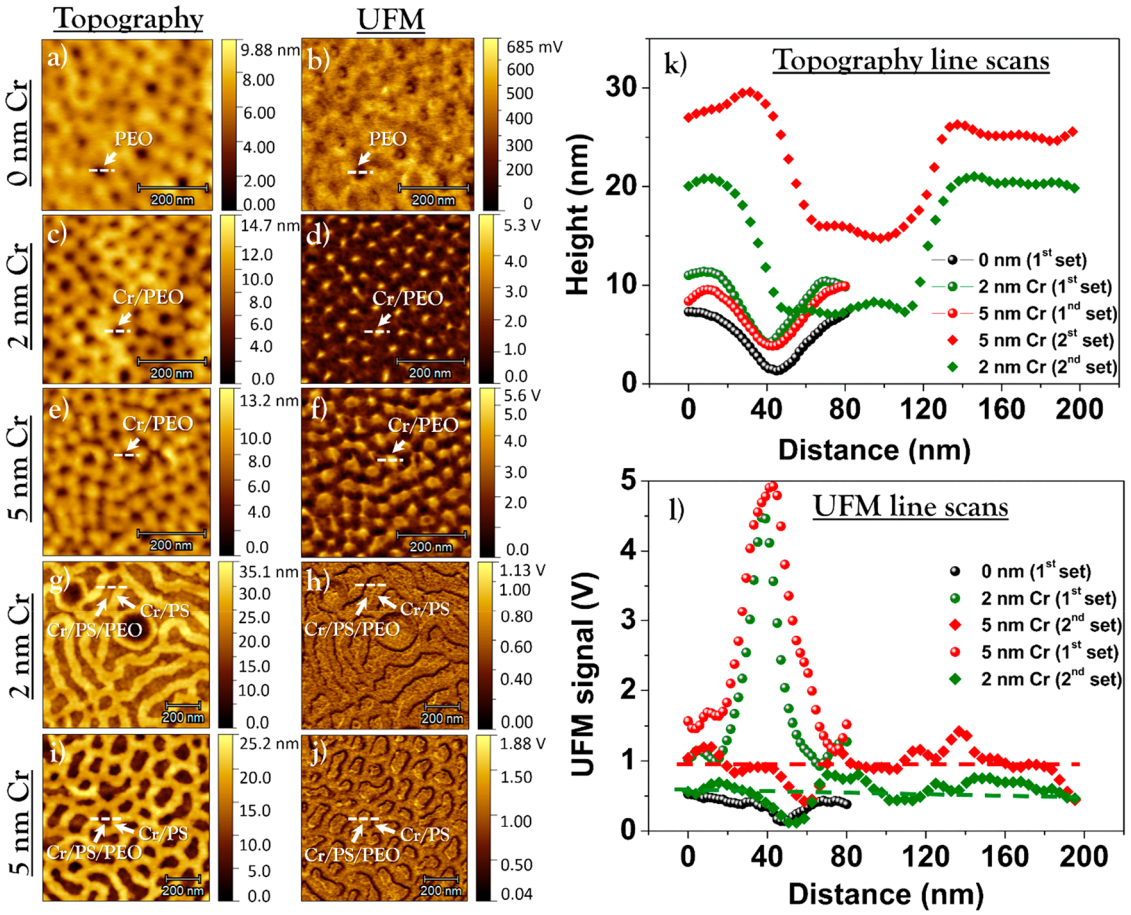

Figure 4. (a, c, e) Topography and (b, d, f) UFM maps of the first set of samples with 0, 2, and 5 nm Cr layer, respectively. (g, i) Topography and (h, j) UFM maps of the second set of samples with 2 and 5 nm Cr layer, respectively. (k) Topography and (l) UFM line scan profiles obtained from the white dashed lines depicted in the topography and UFM images, respectively.

negligible differences in R_{ts} between the first and the second set of samples. The measurements show that by increasing the Cr layer thickness on the BCP films, the thermal resistance, R_{ts}, decreases; thus, the heat transfer from the tip to the sample increases. We have implemented a model to account for the previous point contact measurements and gain more quantitative information regarding the heat transport in the Cr/BCP/Si system. Provided that the point contact measurements were performed at random positions, we have assumed that we can model the BCP film as an equivalent homogeneous layer with effective properties. Details of the heat transport model can be found in the Supporting Information. The blue dashed curve in Figure 3c shows the calculated thermal resistance values. Furthermore, by analyzing the thermal images and taking into account R_t and the power generated in the probe, we estimated the percentage of the thermal resistance variations when the tip is on a surface depression (R_{PEO}) and on the topmost of the surface (R_{PS}) (see the inset graph in Figure 3c).

For the samples with 0 nm Cr, to discern the effect of the BCP thickness modulation from the effect of the difference in thermal conductivity of the two blocks, we have calculated the normalized thermal resistance variation between PS and PEO considering different thicknesses for PS and PEO films (see Table S2). Note that the values presented in Figure 3c include the error derived by topography related changes of the tip−sample contact geometry and film thickness modulations. Although the percentage variation decreases for both sets of samples with increasing the Cr and giving a similar trend, the values are larger in the case of the second set of samples.

Considering the small tip apex of the thermal probe, it is reasonable to assume that the tip−sample thermal exchange is localized at the point contact. Particularly, in high-vacuum experimental conditions the heat transfer through the liquid meniscus and air is eliminated, and neglecting the conductance due to radiation, the dominant heat transfer mechanism is the conduction due to the mechanical contact of the probe with the sample. Here, the heat source size is comparable to the thickness of the Cr layer, and the influence of the Cr layer, with a thermal conductivity 1 order of magnitude larger than the thermal conductivity of the block copolymers, dominates over the substrate. Therefore, the increase of the Cr layer enhances heat dissipation or conductance within the sample giving the trend seen in Figure 3c. In addition, the decrease of the thermal resistance seen in the measurement on the sample with 1 nm Cr layer compared to the measurement on the bare sample indicates that the heat spreading due to the presence of the metal dominates over the Cr−BCP interface thermal resistance.

Finally, the effect of the substrate can also be detected by analyzing the thermal resistance signal obtained from the individual blocks of the bare BCP samples during scanning conditions. This is the case of thermal resistance line profiles in Figure 2e where the variation of the thermal resistance from

DOI: 10.1021/acsapm.9b00924
ACS Appl. Polym. Mater. 2020, 2, 487−496

the topmost of the sample surface to the surface depression is a factor of 3 larger in the case of the sample with horizontally orientated cylinders. It reflects a commensurate variation in the relative height between the topmost of the surface and the surface depression (as seen in the topographic line profile in Figure 2e), which translates to the relative distance between the topmost of the surface and surface depression to the substrate. Therefore, the conductance to the substrate undergoes the detected variations. The different topography between templates persist in the metal covered samples and it is at the origin of the shift between the data in the inset to Figure 3c obtained from the two sets of samples.

Mechanical Analysis of the BCP Templates. To probe nanomechanical properties, UFM measurements were performed in all the samples. UFM uses the standard contact mode capabilities coupled with a high-frequency (~4 MHz) vertical oscillation of the sample substrate (see Figure S9).[54] In addition to the high-frequency oscillation, a sawtooth shape waveform modulates the oscillation at low frequency (~2.7 kHz). As the cantilever (Budget Sensors ContAl-G, 0.2 N m^{-1}) resonant frequency lies around 13 kHz, the tip remains effectively stationary and indents the sample surface with the same amplitude as sample displacement.[54] Then, the tip−sample forces are modulated at high frequency, creating an additional force. Using the intrinsic tip−sample forces vs distance nonlinearity, we detected this additional force, the UFM response, at the low modulation frequency. Therefore, we record the effect of the ultrasonic amplitude on the friction force and the cantilever deflection. The surface stiffness can then be mapped at the nanoscale as the UFM response increases with the material local stiffness.[55] This relationship was shown to hold for a wide range of materials from polymers to semiconductors.[54,56] More details regarding the UFM working principle are shown in the Supporting Information.

Topography and UFM scans performed on both set of BCP samples. In Figure 4, we show UFM maps of the bare BCP without Cr layer and of the metal covered BCP films with 1, 2, and 5 nm Cr. Looking at the noncoated sample (Figure 4b) with the vertical oriented cylinders, we observe bright areas (stiffer materials) corresponding to the PS matrix and dark regions (softer materials) for the PEO cylinders. Even if some discrepancies in the UFM response are recorded, areas highlighted by white arrows are wide compared to the tip dimensions and thus cannot be solely attributed to topography artifacts. These results agree with a larger Young's modulus (E) value obtained for PS (E_{PS} ~ 4 GPa)[57,58] than for PEO (E_{PEO} ~ 0.2 GPa).[59,60] Therefore, the PS appears stiffer in the absence of a covering Cr layer.

The presence of a Cr film on top of the BCP is expected to increase the stiffness of the surface as the Young's modulus of Cr thin films[61] and oxidized Cr[62] is found much larger compared to PS and PEO (E_{Cr} ~ 180 GPa). However, after Cr deposition on the BCP with the vertical oriented cylinders, the nanomechanical behavior of the two polymer blocks is found to be reversed (Figures 4d,f). Instead of probing a lower UFM response in the PEO phase, we observe an inversion of the contrast; e.g., the Cr-covered PS appears softer than the Cr-covered PEO. The inversion of the UFM signal with increasing Cr thickness is shown in the 80 nm long line scans of Figure 4l. The relative change of the UFM signal between PS matrix and PEO cylinders increases more than 1 order of magnitude after Cr evaporation.

The origin of this result can be understood considering the causes giving the growth morphology revealed by the TEM measurements (see first set in Figures 1j,k,l and Figures S5a,b). The difference of the mobility for Cr in PS and PEO produces the coalescence of the Cr islands on the PS block. On the contrary, the same difference in mobility, together with the chemical reactivity in the hydrophilic PEO block, results in an embedding and subsurface growth in the early stages of Cr deposition[30,63,64] and to the formation of metal−oxygen−polymer complexes.[65,66] The latter yields a larger adhesion of the Cr on the PEO block, which results in the apparent increase of the stiffness measured by the UFM.

In the solvent-annealed BCP templates with the 2 and 5 nm Cr layer, the UFM maps show similar stiffness in all the areas of the BCP surface (see Figures 4h,j). This result can be explained taking into account the homogeneous metal deposition on the BCP surface, as is shown in the TEM images (see Figures 1m,n, second set, and Figures S5e,f). Because in these samples the PEO cylinders are embedded in the PS matrix, the UFM response is dominated mostly by the adhesion of Cr on PS. The 200 nm long line scan profiles in Figure 4l show similar measured UFM response in all the areas of the metal-covered films. Small fluctuations of the UFM signals can be attributed to the topography variations in transitions between Cr/PS/PEO and Cr/PS areas.

Last, it is interesting to note that although the UFM measurements allow subsurface investigations of the sample,[55,56] the depth probed is highly dependent on the material under the probe and on size of the contact.[67] As we discussed, the contact diameter is less than the features observed (<10 nm). Therefore, the dominant UFM response will then be provided by the first 10 nm directly under the tip apex. We point out that in general metal atoms have 2 orders of magnitude much higher surface energy compare to the polymers.[64] Therefore, with the presence of Cr, the UFM response is dominated mostly by the Cr layer.

3. CONCLUSIONS

In conclusion, this study addresses structural, thermal, and mechanical characterization of bare BCP and metal-covered BCP films at the nanoscale. Our experimental results demonstrate that combined solvent annealing processes and metal deposition can be used to modify the thermal and nanomechanical properties of BCP-based structures The Cr deposition on top of the BCP film is seen to be determined by the arrangement of the polymer blocks. When PEO is arranged in vertical cylinders, the different surface mobility of Cr in the two blocks, in addition to the enhanced interaction of Cr to PEO, results in a dissimilar metal incorporation. On the contrary, in the solvent-annealed samples, the presence of PS all over the sample surface promotes the formation of a homogeneous metal layer. In the thermal analysis, the SThM signal contrast found in the thermal mapping of the bare and solvent-annealed BCP samples, as well as the enhanced thermal conductance measured in the Cr-coated BCPs, has been quantitatively explained by simulating the heat transfer in such structures. In the first case, the thermal resistance contrast has been seen to be dominated by the modulation of the thickness of the BCP layer over the difference in the thermal conductivity of the two blocks. In the second case, the decrease of the thermal resistance, by a factor of about 2.5, by covering the BCP film with 5 nm of Cr is understood from the opening of a thermal conductance channel in the in-plane direction of

DOI: 10.1021/acsapm.9b00924
ACS Appl. Polym. Mater. 2020, 2, 487−496

the metal layer. Finally, UFM measurements showed an apparent change of the stiffness of the blocks by increasing the thickness of the evaporated metal. PEO domains evolve from being more compliant than PS domains in the bare sample to display an enhanced stiffness with increasing Cr content. This result indicates the different nature of the interaction of Cr with the polymer blocks, which increases the adherence of the metal in PEO and more likely is attributed to the formation of metal−oxygen complexes. This work constitutes a step toward the nanoscale characterization of the thermal and mechanical properties of polymer-based structures showing self-assembly and combination with other materials like metals. The study of these basic physical properties is relevant when the combination of metals and polymers is sought for modifying the polymer properties for applications in lithography or nanoelectronics. Then, the performance of such structures in terms of, for example, dissipation of heat or damage caused by fatigue in the metal−polymer interface may be addressed.

■ ASSOCIATED CONTENT

Supporting Information

The Supporting Information is available free of charge at https://pubs.acs.org/doi/10.1021/acsapm.9b00924.

SThM probe calibration, AFM, TEM, and EDX measurements, thermal maps of Cr-covered BCP templates, heat transport model, spreading resistance model, UFM setup, thermal conductivity measurements with the 3ω setup (PDF)

■ AUTHOR INFORMATION

Corresponding Author

*E-mail: alexandros.elsachat@uam.es.

ORCID

Alexandros El Sachat: 0000-0003-3798-9724
Charalambos Evangeli: 0000-0003-3867-8530
Martin Kreuzer: 0000-0002-7305-5016
Maria R. Rodríguez-Laguna: 0000-0001-5582-1728
Emigdio Chavez: 0000-0002-9783-0806
Marianna Sledzinska: 0000-0001-8592-1121
Clivia M. Sotomayor Torres: 0000-0001-9986-2716
Oleg V. Kolosov: 0000-0003-3278-9643

Present Addresses

A.E.S.: Departamento de Física de la Materia Condensada and Condensed Matter Physics Center (IFIMAC), Facultad de Ciencias, C/Francisco Tomás y Valiente 7, Universidad Autónoma de Madrid, 28049 Madrid, Spain.
M.K.: ALBA Synchrotron Light Source, 08290 Cerdanyola del Valles, Barcelona, Spain.
C.E.: Department of Materials, University of Oxford, Parks Road, OX1 3PH Oxford, UK.

Author Contributions

A.E. and J.S. contributed equally to this work. M.K. and A.E. prepared the samples. J.S., A.E., C.E., A.R., C.S.T., F.A., and O.K. developed the protocols required for SThM and UFM measurements. A.E., J.S., and C.E. performed the SThM and UFM measurements and the data analysis. A.E. performed the AFM, SEM, and TEM measurements. J.S. performed the modeling. M.R.L. and E.C.A. performed the thermal conductivity measurements with the 3ω method. M.S. performed the oxygen plasma etching. The manuscript was written by A.E., J.S., and F.A. All authors contributed with comments to its final version. All authors have given approval to the final version of the manuscript.

Notes

The authors declare no competing financial interest.

■ ACKNOWLEDGMENTS

The authors acknowledge the financial support from the EU FP7 project QUANTIHEAT (Grant No. 604668) and The Royal Society Paul Instrument Fund, EPSRC Grant EP/K023373/1. ICN2 is supported by Spanish MINECO (Severo Ochoa Centers of Excellence Program under Grant SEV-2017-0706 and PHENTOM project under Grant FIS2015-70862-P) and by the Generalitat de Catalunya (Grant 2017SGR806 and the CERCA Program). We thank Prof. Séverine Gomès for a critical reading of the manuscript.

■ REFERENCES

(1) Hamley, I. W. Nanostructure fabrication using block copolymers. *Nanotechnology* **2003**, *14* (10), R39.
(2) Segalman, R. A. Patterning with block copolymer thin films. *Mater. Sci. Eng., R* **2005**, *48* (6), 191−226.
(3) Hawker, C. J.; Russell, T. P. Block Copolymer Lithography: Merging "Bottom-Up" with "Top-Down" Processes. *MRS Bull.* **2005**, *30* (12), 952−966.
(4) Darling, S. B. Directing the self-assembly of block copolymers. *Prog. Polym. Sci.* **2007**, *32* (10), 1152−1204.
(5) Park, C.; Yoon, J.; Thomas, E. L. Enabling nanotechnology with self assembled block copolymer patterns. *Polymer* **2003**, *44* (22), 6725−6760.
(6) Park, M.; Harrison, C.; Chaikin, P. M.; Register, R. A.; Adamson, D. H. Block Copolymer Lithography: Periodic Arrays of ~ 10^{11} Holes in 1 Square Centimeter. *Science* **1997**, *276* (5317), 1401−1404.
(7) Cheng, J. Y.; Ross, C. A.; Chan, V. Z.-H.; Thomas, E. L.; Lammertink, R. G. H.; Vancso, G. J. Formation of a Cobalt Magnetic Dot Array via Block Copolymer Lithography. *Adv. Mater.* **2001**, *13* (15), 1174−1178.
(8) Ghoshal, T.; Senthamaraikannan, R.; Shaw, M. T.; Holmes, J. D.; Morris, M. A. In situ" hard mask materials: a new methodology for creation of vertical silicon nanopillar and nanowire arrays. *Nanoscale* **2012**, *4* (24), 7743−7750.
(9) Lim, J.; Wang, H.-T.; Tang, J.; Andrews, S. C.; So, H.; Lee, J.; Lee, D. H.; Russell, T. P.; Yang, P. Simultaneous Thermoelectric Property Measurement and Incoherent Phonon Transport in Holey Silicon. *ACS Nano* **2016**, *10* (1), 124−132.
(10) Minelli, C.; Hinderling, C.; Heinzelmann, H.; Pugin, R.; Liley, M. Micrometer-Long Gold Nanowires Fabricated Using Block Copolymer Templates. *Langmuir* **2005**, *21* (16), 7080−7082.
(11) Ghoshal, T.; Maity, T.; Senthamaraikannan, R.; Shaw, M. T.; Carolan, P.; Holmes, J. D.; Roy, S.; Morris, M. A. Size and space controlled hexagonal arrays of superparamagnetic iron oxide nanodots: magnetic studies and application. *Sci. Rep.* **2013**, *3*, 2772−2772.
(12) Guarini, K. W.; Black, C. T.; Milkove, K. R.; Sandstrom, R. L. Nanoscale patterning using self-assembled polymers for semiconductor applications. *J. Vac. Sci. Technol., B: Microelectron. Process. Phenom.* **2001**, *19* (6), 2784−2788.
(13) Hong, A. J.; Liu, C.-C.; Wang, Y.; Kim, J.; Xiu, F.; Ji, S.; Zou, J.; Nealey, P. F.; Wang, K. L. Metal Nanodot Memory by Self-Assembled Block Copolymer Lift-Off. *Nano Lett.* **2010**, *10* (1), 224−229.
(14) Cummins, C.; Ghoshal, T.; Holmes, J. D.; Morris, M. A. Strategies for Inorganic Incorporation using Neat Block Copolymer Thin Films for Etch Mask Function and Nanotechnological Application. *Adv. Mater.* **2016**, *28* (27), 5586−5618.
(15) Jin, C.; Olsen, B. C.; Wu, N. L. Y.; Luber, E. J.; Buriak, J. M. Sequential Nanopatterned Block Copolymer Self-Assembly on Surfaces. *Langmuir* **2016**, *32* (23), 5890−5898.

DOI: 10.1021/acsapm.9b00924
ACS Appl. Polym. Mater. 2020, 2, 487−496

(16) Black, C. T. In Integration of self assembly for semiconductor microelectronics, *Proceedings of the IEEE 2005 Custom Integrated Circuits Conference*, 21 Sept 2005; 2005; pp 87−91.
(17) Black, C. T.; Guarini, K. W.; Milkove, K. R.; Baker, S. M.; Russell, T. P.; Tuominen, M. T. Integration of self-assembled diblock copolymers for semiconductor capacitor fabrication. *Appl. Phys. Lett.* **2001**, *79* (3), 409−411.
(18) Naito, K.; Hieda, H.; Sakurai, M.; Kamata, Y.; Asakawa, K. In 2.5-in. disk patterned media prepared by an artificially assisted self-assembling method, *2002 IEEE International Magnetics Conference (INTERMAG)*, 28 April−2 May 2002; 2002; p AB10.
(19) Ben-Sasson, A. J.; Tessler, N. Unraveling the Physics of Vertical Organic Field Effect Transistors through Nanoscale Engineering of a Self-Assembled Transparent Electrode. *Nano Lett.* **2012**, *12* (9), 4729−4733.
(20) Segalman, R. A.; McCulloch, B.; Kirmayer, S.; Urban, J. J. Block Copolymers for Organic Optoelectronics. *Macromolecules* **2009**, *42* (23), 9205−9216.
(21) Lee, Y.; Gomez, E. D. Challenges and Opportunities in the Development of Conjugated Block Copolymers for Photovoltaics. *Macromolecules* **2015**, *48* (20), 7385−7395.
(22) Sarkar, B.; Alexandridis, P. Block copolymer−nanoparticle composites: Structure, functional properties, and processing. *Prog. Polym. Sci.* **2015**, *40*, 33−62.
(23) Stefik, M.; Guldin, S.; Vignolini, S.; Wiesner, U.; Steiner, U. Block copolymer self-assembly for nanophotonics. *Chem. Soc. Rev.* **2015**, *44* (15), 5076−5091.
(24) Xia, S.; Song, L.; Chen, W.; Körstgens, V.; Opel, M.; Schwartzkopf, M.; Roth, S. V.; Müller-Buschbaum, P. Printed Thin Diblock Copolymer Films with Dense Magnetic Nanostructure. *ACS Appl. Mater. Interfaces* **2019**, *11* (24), 21935−21945.
(25) Morkved, T. L.; Wiltzius, P.; Jaeger, H. M.; Grier, D. G.; Witten, T. A. Mesoscopic self-assembly of gold islands on diblock-copolymer films. *Appl. Phys. Lett.* **1994**, *64* (4), 422−424.
(26) Lopes, W. A.; Jaeger, H. M. Hierarchical self-assembly of metal nanostructures on diblock copolymer scaffolds. *Nature* **2001**, *414*, 735.
(27) Kreuzer, M.; Simão, C.; Diaz, A.; Sotomayor Torres, C. M. Formation of Titanium Nanostructures on Block Copolymer Templates with Varying Molecular Weights. *Macromolecules* **2014**, *47* (24), 8691−8699.
(28) Erb, D. J.; Schlage, K.; Röhlsberger, R. Uniform metal nanostructures with long-range order via three-step hierarchical self-assembly. *Sci. Adv.* **2015**, *1* (10), No. e1500751.
(29) Zou, W.; Cai, X.; Li, J.; Dai, X.; Zhang, H.; Zhou, A.; Li, J.; Song, L.; Iyoda, T. Selective deposition on block copolymer film by thermal evaporation of silver. *Surf. Coat. Technol.* **2012**, *206* (22), 4634−4638.
(30) Gensch, M.; Schwartzkopf, M.; Ohm, W.; Brett, C. J.; Pandit, P.; Vayalil, S. K.; Bießmann, L.; Kreuzer, L. P.; Drewes, J.; Polonskyi, O.; Strunskus, T.; Faupel, F.; Stierle, A.; Müller-Buschbaum, P.; Roth, S. V. Correlating Nanostructure, Optical and Electronic Properties of Nanogranular Silver Layers during Polymer-Template-Assisted Sputter Deposition. *ACS Appl. Mater. Interfaces* **2019**, *11* (32), 29416−29426.
(31) Roth, S. V.; Santoro, G.; Risch, J. F. H.; Yu, S.; Schwartzkopf, M.; Boese, T.; Döhrmann, R.; Zhang, P.; Besner, B.; Bremer, P.; Rukser, D.; Rübhausen, M. A.; Terrill, N. J.; Staniec, P. A.; Yao, Y.; Metwalli, E.; Müller-Buschbaum, P. Patterned Diblock Co-Polymer Thin Films as Templates for Advanced Anisotropic Metal Nanostructures. *ACS Appl. Mater. Interfaces* **2015**, *7* (23), 12470−12477.
(32) Zhang, W.; Wu, Z.; Dong, J.; Yan, X.; Gao, W.; Ma, R.; Hou, X. Heat Dissipation Properties of Thin-Film Encapsulation by Insertion of a Metal Thin Film for Organic Light-Emitting Diodes. *Phys. Status Solidi A* **2018**, *215* (23), 1800326.
(33) Dolbin, I. V.; Burya, A. I.; Kozlov, G. V. The structure and thermal stability of polymer materials: A fractal model. *High Temp.* **2007**, *45* (3), 313−316.
(34) George, M. C.; Rodriguez, M. A.; Kent, M. S.; Brennecka, G. L.; Hopkins, P. E. Thermal Conductivity of Self-Assembling Symmetric Block Copolymer Thin Films of Polystyrene-Block-Poly(methyl methacrylate). *J. Heat Transfer* **2016**, *138* (2), 024505−024505.
(35) Chen, J. T.; Thomas, E. L.; Ober, C. K.; Hwang, S. S. Zigzag Morphology of a Poly(styrene-b-hexyl isocyanate) Rod-Coil Block Copolymer. *Macromolecules* **1995**, *28* (5), 1688−1697.
(36) Pryamitsyn, V.; Ganesan, V. Self-assembly of rod−coil block copolymers. *J. Chem. Phys.* **2004**, *120* (12), 5824−5838.
(37) Reenders, M.; ten Brinke, G. Compositional and Orientational Ordering in Rod−Coil Diblock Copolymer Melts. *Macromolecules* **2002**, *35* (8), 3266−3280.
(38) Zauscher, S.; Parlak, Z.; Tu, Q. Mapping the Stiffness of Nanomaterials and Thin Films by Acoustic AFM Techniques: Datasheet from *Handbook of Nanomaterials Properties* in Springer Materials; Springer-Verlag: Berlin.
(39) Jeong, W.; Hur, S.; Meyhofer, E.; Reddy, P. Scanning Probe Microscopy for Thermal Transport Measurements. *Nanoscale Microscale Thermophys. Eng.* **2015**, *19* (4), 279−302.
(40) Mokarian-Tabari, P.; Collins, T. W.; Holmes, J. D.; Morris, M. A. Cyclical "Flipping" of Morphology in Block Copolymer Thin Films. *ACS Nano* **2011**, *5* (6), 4617−4623.
(41) Xu, J.; Hong, S. W.; Gu, W.; Lee, K. Y.; Kuo, D. S.; Xiao, S.; Russell, T. P. Fabrication of Silicon Oxide Nanodots with an Areal Density Beyond 1 Teradots Inch−2. *Adv. Mater.* **2011**, *23* (48), 5755−5761.
(42) Cummins, C.; Mokarian-Tabari, P.; Andreazza, P.; Sinturel, C.; Morris, M. A. Solvothermal Vapor Annealing of Lamellar Poly-(styrene)-*block*-poly(d,l-lactide) Block Copolymer Thin Films for Directed Self-Assembly Application. *ACS Appl. Mater. Interfaces* **2016**, *8* (12), 8295−8304.
(43) Sinturel, C.; Vayer, M.; Morris, M.; Hillmyer, M. A. Solvent Vapor Annealing of Block Polymer Thin Films. *Macromolecules* **2013**, *46* (14), 5399−5415.
(44) Neto, C.; James, M.; Telford, A. M. On the Composition of the Top Layer of Microphase Separated Thin PS-PEO Films. *Macromolecules* **2009**, *42* (13), 4801−4808.
(45) Metwalli, E.; Körstgens, V.; Schlage, K.; Meier, R.; Kaune, G.; Buffet, A.; Couet, S.; Roth, S. V.; Röhlsberger, R.; Müller-Buschbaum, P. Cobalt Nanoparticles Growth on a Block Copolymer Thin Film: A Time-Resolved GISAXS Study. *Langmuir* **2013**, *29* (21), 6331−6340.
(46) Farrell, R. A.; Fitzgerald, T. G.; Borah, D.; Holmes, J. D.; Morris, M. A. Chemical interactions and their role in the microphase separation of block copolymer thin films. *Int. J. Mol. Sci.* **2009**, *10* (9), 3671−3712.
(47) Schwartzkopf, M.; Santoro, G.; Brett, C. J.; Rothkirch, A.; Polonskyi, O.; Hinz, A.; Metwalli, E.; Yao, Y.; Strunskus, T.; Faupel, F.; Müller-Buschbaum, P.; Roth, S. V. Real-Time Monitoring of Morphology and Optical Properties during Sputter Deposition for Tailoring Metal−Polymer Interfaces. *ACS Appl. Mater. Interfaces* **2015**, *7* (24), 13547−13556.
(48) Schwartzkopf, M.; Buffet, A.; Körstgens, V.; Metwalli, E.; Schlage, K.; Benecke, G.; Perlich, J.; Rawolle, M.; Rothkirch, A.; Heidmann, B.; Herzog, G.; Müller-Buschbaum, P.; Röhlsberger, R.; Gehrke, R.; Stribeck, N.; Roth, S. V. From atoms to layers: in situ gold cluster growth kinetics during sputter deposition. *Nanoscale* **2013**, *5* (11), 5053−5062.
(49) Pumarol, M. E.; Rosamond, M. C.; Tovee, P.; Petty, M. C.; Zeze, D. A.; Falko, V.; Kolosov, O. V. Direct Nanoscale Imaging of Ballistic and Diffusive Thermal Transport in Graphene Nanostructures. *Nano Lett.* **2012**, *12* (6), 2906−2911.
(50) Tovee, P.; Pumarol, M.; Zeze, D.; Kjoller, K.; Kolosov, O. Nanoscale spatial resolution probes for scanning thermal microscopy of solid state materials. *J. Appl. Phys.* **2012**, *112* (11), 114317.
(51) El Sachat, A.; Köenemann, F.; Menges, F.; Del Corro, E.; Garrido, J. A.; Sotomayor Torres, C. M.; Alzina, F.; Gotsmann, B. Crossover from ballistic to diffusive thermal transport in suspended graphene membranes. *2D Mater.* **2019**, *6* (2), 025034.

DOI: 10.1021/acsapm.9b00924
ACS Appl. Polym. Mater. 2020, 2, 487−496

(52) Menges, F.; Riel, H.; Stemmer, A.; Dimitrakopoulos, C.; Gotsmann, B. Thermal transport into graphene through nanoscopic contacts. *Phys. Rev. Lett.* **2013**, *111* (20), 205901.
(53) Steffes, J. J.; Ristau, R. A.; Ramesh, R.; Huey, B. D. Thickness scaling of ferroelectricity in $BiFeO_3$ by tomographic atomic force microscopy. *Proc. Natl. Acad. Sci. U. S. A.* **2019**, *116* (7), 2413−2418.
(54) Dinelli, F.; Biswas, S. K.; Briggs, G. A. D.; Kolosov, O. V. Ultrasound induced lubricity in microscopic contact. *Appl. Phys. Lett.* **1997**, *71* (9), 1177−1179.
(55) Kolosov, O.; Briggs, A. Ultrasonic Force Microscopies. In *Acoustic Scanning Probe Microscopy*; Marinello, F., Passeri, D., Savio, E., Eds.; Springer: Berlin, 2013; pp 261−292.
(56) Bosse, J. L.; Timofeeva, M.; Tovee, P. D.; Robinson, B. J.; Huey, B. D.; Kolosov, O. V. Nanothermal characterization of amorphous and crystalline phases in chalcogenide thin films with scanning thermal microscopy. *J. Appl. Phys.* **2014**, *116* (13), 134904.
(57) Briscoe, B. J.; Fiori, L.; Pelillo, E. Nano-indentation of polymeric surfaces. *J. Phys. D: Appl. Phys.* **1998**, *31* (19), 2395.
(58) Lubarsky, G. V.; Davidson, M. R.; Bradley, R. H. Elastic modulus, oxidation depth and adhesion force of surface modified polystyrene studied by AFM and XPS. *Surf. Sci.* **2004**, *558* (1), 135−144.
(59) Dinelli, F.; Pingue, P.; Kay, N. D; Kolosov, O. V Subsurface imaging of two-dimensional materials at the nanoscale. *Nanotechnology* **2017**, *28* (8), 085706.
(60) Nie, H. Y.; Motomatsu, M.; Mizutani, W.; Tokumoto, H. Local modification of elastic properties of polystyrene−polyethyleneoxide blend surfaces. *J. Vac. Sci. Technol., B: Microelectron. Process. Phenom.* **1995**, *13* (3), 1163−1166.
(61) Petersen, K. E.; Guarnieri, C. R. Young's modulus measurements of thin films using micromechanics. *J. Appl. Phys.* **1979**, *50* (11), 6761−6766.
(62) Lahoche, L.; Lorman, V.; Rochal, S. B.; Roelandt, J. M. Effect of the Ordering of Metal/Oxide Interface on the Thermomechanical Behaviour of High Temperature Oxidized Metal Films. *Mater. Sci. Forum* **1997**, *251−254*, 459−466.
(63) Yu, S.; Santoro, G.; Sarkar, K.; Dicke, B.; Wessels, P.; Bommel, S.; Döhrmann, R.; Perlich, J.; Kuhlmann, M.; Metwalli, E.; Risch, J. F. H.; Schwartzkopf, M.; Drescher, M.; Müller-Buschbaum, P.; Roth, S. V. Formation of Al Nanostructures on Alq3: An in Situ Grazing Incidence Small Angle X-ray Scattering Study during Radio Frequency Sputter Deposition. *J. Phys. Chem. Lett.* **2013**, *4* (18), 3170−3175.
(64) Torrisi, V.; Ruffino, F. J. C. Metal-polymer nanocomposites: (Co-) evaporation/(Co) sputtering approaches and electrical properties. *Coatings* **2015**, *5* (3), 378−424.
(65) Burkstrand, J. M. Formation of metal−oxygen−polymer complexes on polystyrene with nickel and chromium. *J. Vac. Sci. Technol.* **1979**, *16* (4), 1072−1074.
(66) Friedrich, J. F.; Koprinarov, I.; Giebler, R.; Lippitz, A.; Unger, W. E. S. Reactions and Intermediates at the Metal-Polymer Interface as Observed by XPS and NEXAFS Spectroscopy. *J. Adhes.* **1999**, *71* (2−3), 297−321.
(67) Briggs, A.; Kolosov, O. *Acoustic Microscopy*, 2nd ed.; 2010; pp 1−384.

DOI: 10.1021/acsapm.9b00924
ACS Appl. Polym. Mater. 2020, 2, 487−496